A Novel Choke-Less Class-E Inverter with Multiplexed Transmitter Coil for Inductive Power Transfer

Jingyu Wang, Hai Xu, *Member, IEEE*, Zhicong Huang, *Senior Member, IEEE*, Chi-Kwan Lee, *Senior Member, IEEE*, Io-Wa Iam, *Member, IEEE*, and Chi-Seng Lam, *Senior Member, IEEE*.

***Abstract*—Current Class-E inverters for Inductive Power Transfer (IPT) inevitably incorporate inductors. Especially, when realizing constant current source excitation for the transmitting coils, more inductors are often required. To address this limitation, this paper proposes a novel choke-less Class-E inverter specifically designed for IPT systems with dual transmitting coils. Unlike the operating mode of traditional Class-E inverters, the proposed method multiplexes the dual transmitting coils as inductors, completing the charging and discharging of the passive components while achieving quasi-constant current source excitation for the dual transmitting coils. Thus, the proposed method eliminates the inductors in the Class-E inverter and introduces the inherent advantages of the dual transmitting coil configuration. The paper details the operating principle and derives the equivalent circuit model for the IPT system based on this novel inductor-less Class-E inverter. The parameter design ensures that both the zero-voltage switching (ZVS) condition and the output characteristic are load-independent, thereby minimizing the need for complex control to eliminate the control effort. Experiment results validate the proposed design.**

***Index Terms*—Choke-less, Class-E Inverter, Inductive Power Transfer, Multiplex, Zero Voltage Switching, Load-Independent Output.**

I. INTRODUCTION

Manuscript submitted MONTH XX, 2025. This work was supported in part by the National Natural Science Foundation of China under Grant 52577198, in part by the Guangzhou Municipal Science and Technology Bureau under Grant 2025A04J7064, in part by the Fundamental Research Funds for the Central Universities, in part by the Science and Technology Planning Project of Guangdong Province under Grant 2025A0505010015, in part by The Science and Technology Development Fund, Macau SAR (FDCT) under Grant 0187/2024/AGJ, Grant 0110/2024/RIB2, Grant 0106/2025/RIB2, and Grant 0001/2025/NRP, and in part by the University of Macau under Grant MYRG-GRG2024-00086-IME. (Corresponding author: Zhicong Huang)

Jingyu Wang is with the School of Electrical Engineering, Qingdao University, Qingdao, China. (e-mail: qduwjy@qdu.edu.cn).

Hai Xu was with the Shien-Ming Wu School of Intelligent Engineering, South China University of Technology, Guangzhou 510006, China, and now is with the Department of Electrical and Electronic Engineering, The Hong Kong Polytechnic University, Hong Kong, China. (e-mail: haixu@polyu.edu.hk).

Zhicong Huang is with the Shien-Ming Wu School of Intelligent Engineering, South China University of Technology, Guangzhou 510006, China. (e-mail: zhiconghuang@scut.edu.cn).

Chi-Kwan Lee is with the School of Electrical and Data Engineering, University of Technology Sydney, Ultimo, NSW, Australia. (email: chikwan.lee@uts.edu.au).

Io-Wa Iam and Chi-Seng Lam are with the State Key Laboratory of Analog and Mixed-Signal VLSI, University of Macau, Macau 999078, China, and also with the Institute of Microelectronics, University of Macau, Macau 999078, China. (e-mail: iwiam@um.edu.mo, cslam@um.edu.mo).

Chi-Seng Lam is also with the Department of Microelectronics, Faculty of Information Science and Computing, University of Macau, Macau 999078, China.

INDUCTIVE power transfer (IPT) stands out as an exceptional method for power transfer, offering the advantages of being contactless, safe, and convenient [1], [2]. Its versatility spans a wide range of applications and power levels, including consumer electronics [3], [4], biomedical implants [5], [6], and electric vehicles [7]–[11].

Due to their flexible modulation and high power output capabilities, most research on IPT focuses on Full-Bridge (FB) and Half-Bridge (HB) topologies [12], [13]. However, for low-power IPT applications, bridgeless converters offer notable advantages, including fewer semiconductor devices and simpler driving circuits. Furthermore, advancements in wide-bandgap semiconductor technologies are driving power electronic converters towards higher voltages, higher frequencies, and more compact designs. The structural characteristics of bridgeless converters, which eliminate the risk of shoot-through issues, make them particularly well-suited for high-frequency applications [14]–[16].

Various bridgeless converters have been explored in previous research, including forward resonant converters, quasi-resonant flyback converters, and Class-E family converters [17]–[20]. However, in IPT applications, these topologies face specific challenges. The forward resonant converter struggles with the uncompensated magnetizing inductance of the transformer [17], while the quasi-resonant flyback converter is affected by large leakage inductance [18]. Conversely, the Class E-derived converter has emerged as the preferred bridgeless topology, particularly for low-power and high-frequency IPT applications [19], [20].

In the IPT application, the load-independent output characteristic of the Class-E inverter could eliminate the need for complex closed-loop control to stabilize the output voltage, which greatly enhances its practicability in IPT applications [21]–[23]. Sometimes the transmitting coil is preferred to be excited with a constant current (CC) power source to deal with the removal and the open-circuit of the receiving coils. At present, some studies focus on the Class-E inverter with CC load-independent output in IPT applications.

First, the choke-inductor-based Class-E type IPT inverter is studied in [24]–[27]. The Class-EF inverter with CC output is discussed in [24], [25]. This method derives the phase relationship of the output current required for Class EF inverters to achieve CC output and adjusts the capacitance parameters in the circuit to achieve CC output and zero-voltage switching (ZVS). However, this method has a choke inductor and a

TABLE I
A COMPARISON OF CLASS-E INVERTERS FOR CONSTANT CURRENT OUTPUT

References	Topology	Choke inductors	Resonant inductors	Percentage of PCB area occupied by inductors	Frequency	Output power	DC-DC Efficiency
[25]	Class-EF	1	1	8%	6.78 Mhz	56 W	90.0%
[26]	Inverse Class-E	1	1	16.6%	3.39 Mhz	75 W	88.0%
[28]	Class-E	0	2	31.5%	100 kHz	11 W	86.4%
[30]	Class-Φ2	1	2	60%	6.78 Mhz	350 W	91.0%
Proposed	Class-E	0	0	0	1 Mhz	100 W	93.2%

resonant inductor on the PCB of the transmitting circuit. Based on the above method, the inverse Class-E inverter with CC output and zero current switching (ZCS) is discussed in [26], [27]. Compared with the converter in [24], [25], this method could realize ZCS and low total harmonic distortion (THD). However, this method did not reduce the number of inductors.

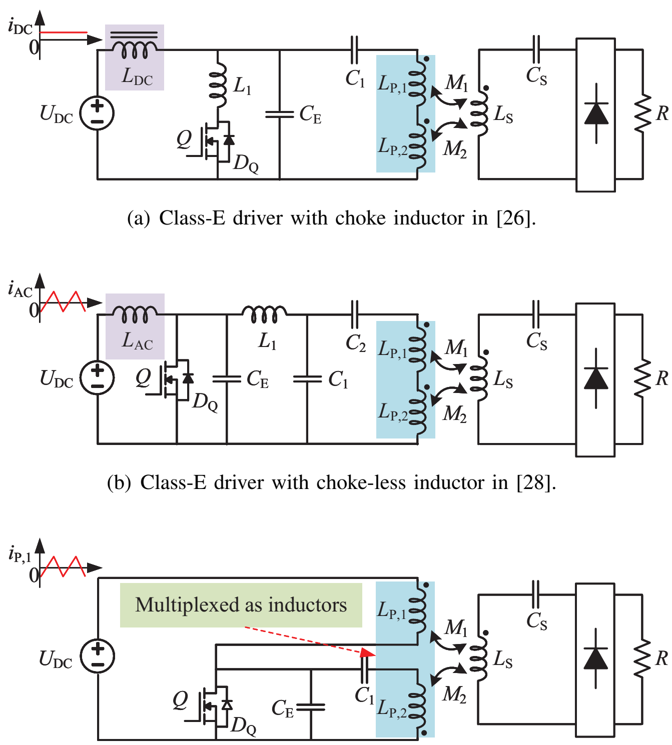

(a) Class-E driver with choke inductor in [26].

(b) Class-E driver with choke-less inductor in [28].

(c) Proposed Class-E driver.

Fig. 1. Comparison of Class-E drivers for IPT to drive dual transmitting coils.

To avoid using the choke inductor and provide a wider range of load-independent output capabilities, choke-less-based Class-E inverters are studied in [21]. These studies replaced the choke inductor with a resonant inductor and reconstructed the working mode of Class-E inverters. On this basis, the extra LCC compensation network is added in this kind of inverter to realize load-independent CC output [28], [29]. Similarly, this method can also be applied to Class-Φ to achieve the CC output of the inverter [30]. Although this method reduces the inductance value, the two resonant inductors still occupy considerable space in the transmitting circuit.

In order to further eliminate inductors in Class-E circuits, this paper proposes a novel choke-less Class-E inverter as shown in Fig. 1(c). Unlike the operating mode of the above Class-E inverters, the proposed method multiplexes the dual transmitting coils as inductors, completing the charging and discharging of the passive components while achieving quasi-constant current source excitation for the dual transmitting coils. Compared with the aforementioned methods, on the one hand, the proposed method eliminates the inductors in the circuit, resulting in a more compact circuit structure. On the other hand, it directly drives the dual-coil structure. And the dual-coils, such as BPP and DDQP, have been proven to have better lateral misalignment as discussed in [31]–[34].

As shown in Fig. 1, to more fairly demonstrate the advantages of the proposed method, this paper, with the goal of implementing a constant current source to drive the dual transmitting coils, compares the implementation schemes for IPT of Class-E circuits based on choke-inductor-based, choke-less-based, and proposed approaches. In addition, this paper provides Table I for a more detailed parameter comparison. Under the premise of the aforementioned goal, based on the results of the comprehensive comparisons, the proposed design eliminates the inductor, significantly reducing the inverter size while retaining the advantages of a Class-E inverter—compactness, light weight, soft switching, high-frequency operation, and high efficiency. Removing the bulky magnetic component brings several benefits, including lower component cost, reduced weight, and lower volume.

This paper first elaborates on the operating principle and derives the equivalent circuit model for the IPT system based on this novel inductor-less Class-E inverter. It then deduces the zero-voltage switching (ZVS) realization conditions and establishes the output model of the Class-E inverter. In addition, the parameter design ensures that both the ZVS condition and output characteristics are load-independent, thereby minimizing the requirement for complex control and reducing control effort. Finally, the correctness of the theoretical analysis has been verified through simulations and experiments.

II. PROPOSED CIRCUIT TOPOLOGY AND OPERATING PRINCIPLE

A. Schematic of the Proposed System

This paper proposes a novel Class-E IPT converter that uses multiplexed resonant inductors and transmitting coils. In this design, a transmitting coil, $L_{\mathrm{P},1}$, replaces the traditional choke inductor. The proposed converter's schematic is illustrated in Fig. 2. The Class-E driver includes a DC voltage source U_{DC}, a MOSFET switch Q, two transmitting coils, and their respective compensation capacitors. The self-inductances of the two transmitting coils, $L_{\mathrm{P},1}$ and $L_{\mathrm{P},2}$, are

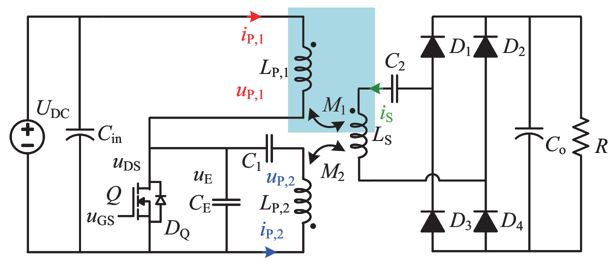

Fig. 2. Proposed Class-E IPT circuit.

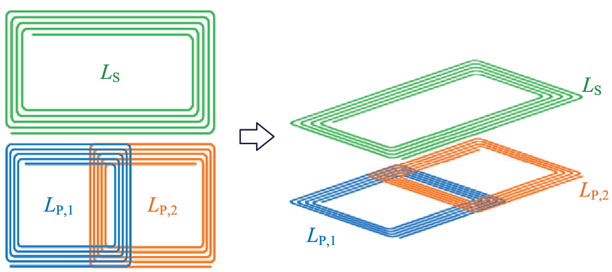

Fig. 3. The structure of BP-type coil.

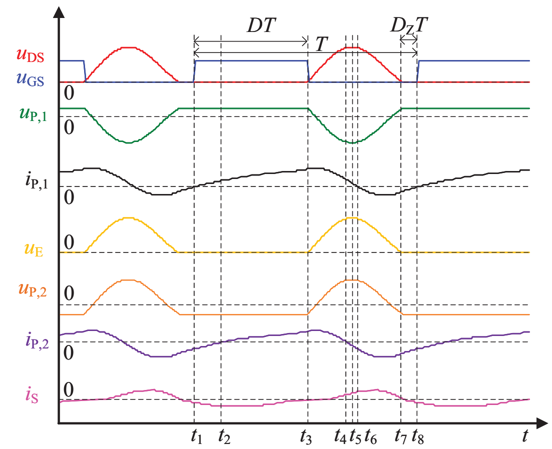

Fig. 4. The operation waveforms of the proposed circuit.

decoupled, with capacitors C_{E} used for their compensation. Capacitor C_1 isolates the DC component. The receiving coil, with self-inductance L_{S}, is coupled with the two transmitting coils, establishing a loosely coupled transformer with mutual inductances M_1 and M_2. Capacitor C_2 provides compensation in the receiving circuit, while a rectifier converts AC to DC power to supply a load with resistance R.

The proposed circuit utilizes a BP-type coil, as illustrated in Fig. 3. The transmitting coils comprise two identical, partially overlapping coils, $L_{\mathrm{P},1}$ and $L_{\mathrm{P},2}$, where $L_{\mathrm{P},1} = L_{\mathrm{P},2} = L_{\mathrm{P}}$. According to the conditions described in [34], when coils $L_{\mathrm{P},1}$ and $L_{\mathrm{P},2}$ are positioned as specified, they are effectively decoupled from each other, resulting in a mutual inductance of $M_{12} = 0$.

B. Operation Principle

The key waveforms of the proposed circuit are illustrated in Fig. 4, u_{GS} and u_{DS} denote the gate-source and drain-source voltages of Q, respectively. $i_{\mathrm{P},1}$ and $i_{\mathrm{P},2}$ represent the currents through the transmitting coils $L_{\mathrm{P},1}$ and $L_{\mathrm{P},2}$. $u_{\mathrm{P},1}$ and $u_{\mathrm{P},2}$ are the voltages across these transmitting coils. U_{E} indicates the voltage across the compensation capacitor C_{E}, while i_{S} is the current through the receiving coil. D stands for the duty cycle of Q, D_{Z} is the dead time ratio, and T is the switching period.

The operation of the proposed two-coil driving circuit is segmented into seven distinct modes, as depicted in Fig. 4 and detailed in Fig. 5. The sequence of these modes is outlined as follows:

$Model$ 1 $[t_1-t_2]$: At time t_1, the switch Q is turned on. The voltage of the transmitting coil $L_{\mathrm{P},1}$ is clamped to U_{DC}, while the voltage of the capacitor C_{E} is clamped to zero. With the input voltage charging the transmitting coil $L_{\mathrm{P},1}$ through Q, the current of the transmitting $L_{\mathrm{P},1}$ gradually rises from zero. The transmitting coil $L_{\mathrm{P},2}$ follows current through capacitor C_1 and Q. At time t_2, the current $i_{\mathrm{P},2}$ gradually decreases to zero.

$Mode$ 2 $[t_2-t_3]$: Both the currents $i_{\mathrm{P},1}$ and $i_{\mathrm{P},2}$ increase gradually. At the time t_3, the switch Q is turned off, currents $i_{\mathrm{P},1}$ and $i_{\mathrm{P},2}$ increases to approach the maximum.

$Mode$ 3 $[t_3-t_4]$: The capacitor C_{E} is charged by the coil $L_{\mathrm{P},1}$ and coil $L_{\mathrm{P},2}$. Both the currents $i_{\mathrm{P},1}$ and $i_{\mathrm{P},2}$ decrease gradually. At time t_4, the current $i_{\mathrm{P},2}$ gradually decrease to zero.

$Mode$ 4 $[t_4-t_5]$: The capacitor C_{E} and coil $L_{\mathrm{P},2}$ is charged by the coil $L_{\mathrm{P},1}$, the current $i_{\mathrm{P},2}$ gradually increases from zero. At the time t_5, the charging current of C_{E} decreases to zero, and the voltage U_{E} approaches the maximum.

$Mode$ 5 $[t_5-t_6]$: The capacitor C_{E} is discharged. And the coil $i_{\mathrm{P},2}$ is charged by the capacitor C_{E} and the coil $L_{\mathrm{P},1}$. At time t_6, the current $i_{\mathrm{P},1}$ gradually decreases to zero.

$Mode$ 6 $[t_6-t_7]$: The coil $L_{\mathrm{P},1}$ and $L_{\mathrm{P},2}$ is charging by the capacitor C_{E}. At time t_7, the voltage $u_{\mathrm{P},1}$ gradually increases to the U_{DC}, and the voltage U_{E} gradually decreases to zero.

$Mode$ 7 $[t_7-t_8]$: Due to the voltages $u_{\mathrm{P},1}$ and U_{E} are clamped, the diode D_{Q} is forced to conduct and the coils $L_{\mathrm{P},1}$ and $L_{\mathrm{P},2}$ are discharged through D_{Q}. The voltage on the switch u_{DS} is zero until the switch is turned on. The ZVS of the switch is realized.

C. Equivalent Circuit

The establishment of an equivalent circuit requires the following three steps:

1) Operation status analysis: Due to the large value of C_1, as illustrated in Fig. 6, when switch Q is turned on, the voltage across $L_{\mathrm{P},1}$ is clamped to U_{DC}, while the voltage across $L_{\mathrm{P},2}$ is clamped to $-U_{\mathrm{DC}}$, which is the voltage of C_1. The resistors $R_{\mathrm{S},1}$ and $R_{\mathrm{S},2}$ represent the reflected resistances of the receiving circuit.

The $R_{\mathrm{S,n}}$ can be expressed as:

$$R_{\mathrm{S,n}} = \frac{\omega_{\mathrm{s}}^2 {M_{\mathrm{n}}}^2}{R_{\mathrm{eq}}}, \mathrm{n} = 1or2, \tag{1}$$

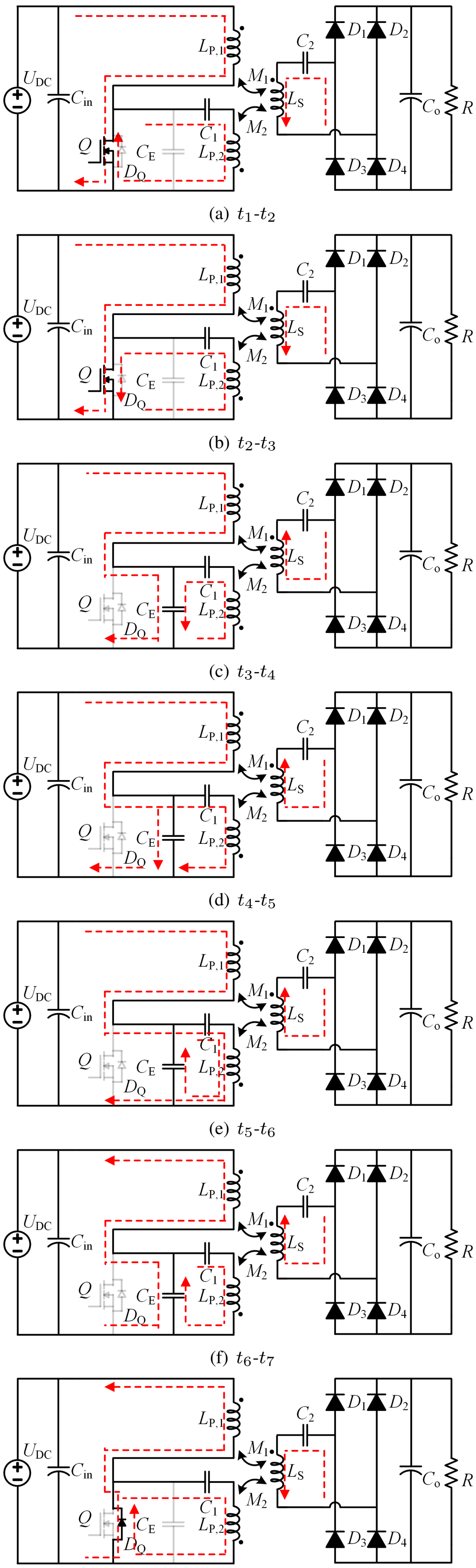

(a) t_1-t_2

(b) t_2-t_3

(c) t_3-t_4

(d) t_4-t_5

(e) t_5-t_6

(f) t_6-t_7

(g) t_7-t_8

Fig. 5. Operating modes of the proposed circuit

where the R_{eq} represents the AC equivalent resistance and can be expressed as:

$$R_{eq} = \frac{8R}{\pi^2}. \tag{2}$$

When switch Q is turned off, as shown in Fig. 7, the transmitting coils $L_{P,1}$ and $L_{P,2}$ resonate with their respective portions of the capacitor C_E. Specifically, $L_{P,1}$ and $C_{E,1}$ form an active series circuit, while $L_{P,2}$ and $C_{E,2}$ form a passive series circuit. The currents $i_{P,1}$ and $i_{P,2}$ can be described by (3). This analysis demonstrates that both $L_{P,1}$ and $L_{P,2}$ have their own oscillation circuits and can facilitate wireless power transfer. Moreover, since $L_{P,1} = L_{P,2}$ in this setup, the current waveforms of $L_{P,1}$ and $L_{P,2}$ are identical, allowing them to drive a single receiving coil jointly.

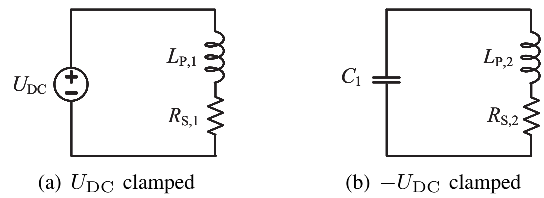

(a) U_{DC} clamped (b) $-U_{DC}$ clamped

Fig. 6. Equivalent circuit model when the switch is turned on.

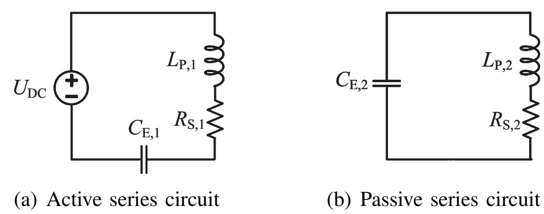

(a) Active series circuit (b) Passive series circuit

Fig. 7. Equivalent circuit model when the switch is turned off.

$$\begin{cases} i_{P,1} = C_{E,1}\frac{du_E(t)}{dt}, \\ i_{P,2} = C_{E,2}\frac{du_E(t)}{dt}. \end{cases} \tag{3}$$

2) Equivalent input voltage: As depicted in Fig. 4, when Q is conducting in either the forward or reverse mode, the voltage across $L_{P,1}$, denoted as $u_{P,1}$, is clamped to the DC voltage source U_{DC}. When Q is off, the circuit exhibits a source-free response, and $u_{P,1}$ becomes underdamped. Based on this operating principle, the relationship between $u_{P,1}$ and u_E is described by (4).

$$u_E(t) = U_{DC} - u_{P,1}(t). \tag{4}$$

Due to C_1 isolating the DC component in u_E, the voltage of $L_{P,2}$ can be expressed as

$$u_{P,2}(t) = u_E(t) - U_{DC} = -u_{P,1}(t). \tag{5}$$

3) Simplify the circuit: Based on (5), the circuit simplification process is shown in Fig. 8.

According to Fig. 8, the equivalent circuit of the proposed converter is shown in Fig. 9. The $i_P = i_{P,1} + i_{P,2}$.

$$
\begin{cases}
R_{\mathrm{E}} = \dfrac{R_{\mathrm{S},1}R_{\mathrm{S},2}(R_{\mathrm{S},1}+R_{\mathrm{S},2}) + \omega_{\mathrm{s}}^2(R_{\mathrm{S},1}L_{\mathrm{P},1}^2 + R_{\mathrm{S},2}L_{\mathrm{P},2}^2)}{\omega_{\mathrm{s}}^2(L_{\mathrm{P},1}+L_{\mathrm{P},2})^2 + (R_{\mathrm{S},1}+R_{\mathrm{S},2})^2}, \\
L_{\mathrm{E}} = \dfrac{R_{\mathrm{S},1}^2 L_{\mathrm{P},1} + R_{\mathrm{S},2}^2 L_{\mathrm{P},2} + \omega_{\mathrm{s}}^2 L_{\mathrm{P},1}L_{\mathrm{P},2}(L_{\mathrm{P},1}+L_{\mathrm{P},2})}{\omega_{\mathrm{s}}^2(L_{\mathrm{P},1}+L_{\mathrm{P},2})^2 + (R_{\mathrm{S},1}+R_{\mathrm{S},2})^2}.
\end{cases}
\tag{6}
$$

and

$$
\begin{cases}
R_{\mathrm{E}} \approx \dfrac{R_{\mathrm{S},1}L_{\mathrm{P},1}^2 + R_{\mathrm{S},2}L_{\mathrm{P},2}^2}{(L_{\mathrm{P},1}+L_{\mathrm{P},2})^2}, \\
L_{\mathrm{E}} \approx \dfrac{L_{\mathrm{P},1}L_{\mathrm{P},2}}{L_{\mathrm{P},1}+L_{\mathrm{P},2}}.
\end{cases}
\tag{7}
$$

The equivalent mutual inductance can be expressed as (8).

$$
M_{\mathrm{E}} = M_1\frac{R_{\mathrm{E}} + j\omega_{\mathrm{s}}L_{\mathrm{E}}}{R_{\mathrm{S},1} + j\omega_{\mathrm{s}}L_{\mathrm{P},1}} + M_2\frac{R_{\mathrm{E}} + j\omega_{\mathrm{s}}L_{\mathrm{E}}}{R_{\mathrm{S},2} + j\omega_{\mathrm{s}}L_{\mathrm{P},2}}. \tag{8}
$$

Furthermore, it can be expressed as:

$$
M_{\mathrm{E}} \approx M_1\frac{L_{\mathrm{E}}}{L_{\mathrm{P},1}} + M_2\frac{L_{\mathrm{E}}}{L_{\mathrm{P},2}}. \tag{9}
$$

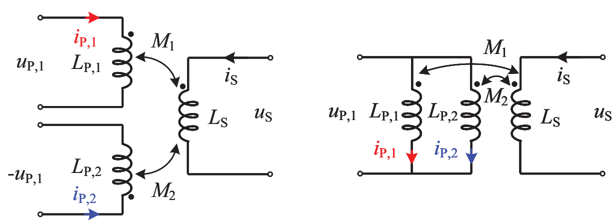

(a) Original circuit (b) Simplified circuit

Fig. 8. Simplified analysis of the inverter output.

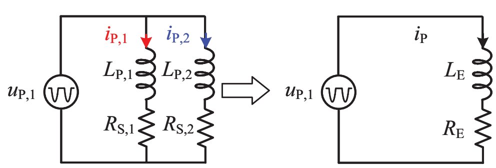

Fig. 9. Simplest equivalent circuit of the inverter output.

III. Zero Voltage Switching Analysis and the Modeling of the Proposed Inverter's Output

A. *Output of the Proposed Inverter*

Based on the equation (5), solving $u_{\mathrm{P},1}$ can obtain the inputs for two coils $L_{\mathrm{P},1}$ and $L_{\mathrm{P},2}$.

The operating waveforms of the proposed IPT driver within a cycle are shown in Fig. 10. And the operating waveform of $u_{\mathrm{P},1}(t)$ can be divided into two modes, i.e., a *DC clamped mode* and an *underdamped mode*. To analyze the fundamental harmonic component of $u_{\mathrm{P},1}$, a two-step simplification of the operating waveforms is carried out as follows.

1) The waveform of $u_{\mathrm{P},1}$ in the underdamped mode can be approximated as a portion of a sinusoid, as shown

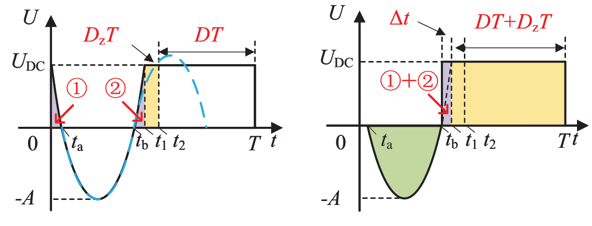

(a) Sinusoidal approximation (b) Wave re-shaping

Fig. 10. Simplification of the waveform of $u_{\mathrm{P},1}(t)$ for calculation.

in Fig. 10(a). Such that, $u_{\mathrm{P},1}$ can be expressed as a piecewise function given by

$$
u_{\mathrm{P},1}(t) = \begin{cases} -A\sin(\omega_0 t + \varphi), & 0 \le t < t_1 \\ U_{\mathrm{DC}}, & t_1 \le t \le T \end{cases} \tag{10}
$$

where A, ω_0, and φ are the amplitude, frequency, and phase angle of the sinusoid, respectively. Since $u_{\mathrm{P},1}$ is a periodic waveform, $u_{\mathrm{P},1}(0) = U_{\mathrm{DC}}$ can be derived.

2) The waveform of $u_{\mathrm{P},1}$ in the short intervals (0, t_{a}) and (t_{b}, t_1) can be linearized, such that sections ① and ② can be approximated as triangles. The duration of these two intervals is identical, denoted as Δt and can be calculated by

$$
\Delta t = t_a - 0 = t_1 - t_b = \frac{\pi \arcsin(\frac{U_{\mathrm{DC}}}{A})}{180\mathrm{deg}\,\omega_0}. \tag{11}
$$

As shown in Fig. 10(b), sections ① and ② can be merged as a rectangular section ① + ②. Such that, $u_{\mathrm{P},1}$ can be reshaped as a new waveform to simplify the calculation and expressed as

$$
u_{\mathrm{P},1}(t) = \begin{cases} 0, & 0 \le t < t_{\mathrm{a}} \\ -A\sin[\omega_0(t - t_{\mathrm{a}})], & t_{\mathrm{a}} \le t < t_{\mathrm{b}} \\ U_{\mathrm{DC}}. & t_{\mathrm{b}} \le t \le T \end{cases} \tag{12}
$$

To obtain the amplitude of arbitrary harmonics of $u_{\mathrm{P},1}(t)$, ω_0 and A should be calculated first.

According to the above analysis, ω_0 could be expressed by

$$
\omega_0 = \frac{\pi}{t_{\mathrm{b}} - t_{\mathrm{a}}} = \frac{\pi}{(1 - D - D_{\mathrm{Z}})T - 2\Delta t}, \tag{13}
$$

where D is the duty cycle of switch Q and D_{Z} is the ZVS margin of the switch.

When calculating A, the principle of voltage-second balance on $L_{\mathrm{P},1}$ within a cycle should be applied:

$$
U_{\mathrm{DC}}(T - t_{\mathrm{b}}) = \int_{t_{\mathrm{a}}}^{t_{\mathrm{b}}} A\sin[\omega_0(t - t_{\mathrm{a}})]\mathrm{d}t = \frac{2A}{\pi}(t_{\mathrm{b}} - t_{\mathrm{a}}). \tag{14}
$$

With (12), (13) and (14), A can be derived as

$$
A = \frac{\pi U_{\mathrm{DC}}\left[(D + D_{\mathrm{Z}})T + \Delta t\right]}{2\left[(1 - D - D_{\mathrm{Z}})T - 2\Delta t\right]}. \tag{15}
$$

After obtaining both ω_0 and A, the curve in Fig. 10(b) can be decomposed into its Fourier components, as given by (16).

$$
u_{\mathrm{P},1}(t) = \sum_{n=1}^{\infty}[a_n\cos(n\omega_{\mathrm{s}}t) + b_n\sin(n\omega_{\mathrm{s}}t)], \tag{16}
$$

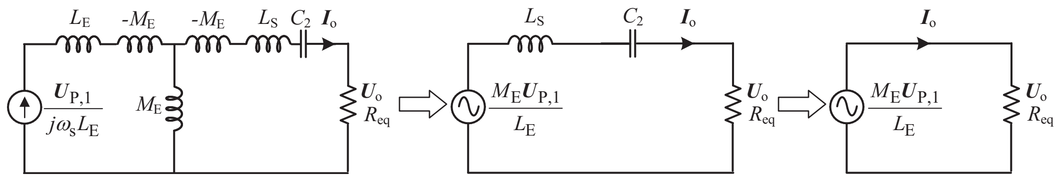

Fig. 11. Thevenin's and Norton's equivalence of the equivalent circuit.

$$a_n = \frac{2}{T}\int_{t_a}^{t_b}(-A)\sin(\omega_0 t)\sin(n\omega_s t)dt + \frac{2}{T}\int_{t_b}^{T}U_{DC}\sin(n\omega_s t)dt, \tag{17a}$$

$$b_n = \frac{2}{T}\int_{t_a}^{t_b}(-A)\sin(\omega_0 t)\cos(n\omega_s t)dt + \frac{2}{T}\int_{t_b}^{T}U_{DC}\cos(n\omega_s t)dt. \tag{17b}$$

where a_n and b_n are calculated by equations (17a) and (17b), respectively.

Therefore, the amplitude of fundamental harmonic of $u_{P,1}$ can be expressed as

$$E = \sqrt{a_1^2 + b_1^2}. \tag{18}$$

According to the above analysis, the value of E is determined by the U_{DC}, D, and ω_0. Based on the analysis in Section II, it can be concluded that E is approximately load independent.

B. Zero Voltage Switching Analysis

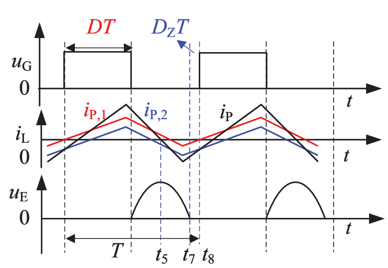

Fig. 12. Key waveforms of ZVS.

In the proposed Class-E IPT converter, ensuring zero-voltage switching (ZVS) requires that $i_P(t_8) \leq 0$, as depicted in Fig. 12. However, this is not the only condition. It is evident that when condition $i_P \leq 0$ is satisfied, U_E may still be greater than 0. Therefore, the analysis of ZVS must also be based on the waveform of U_E. The waveform of U_E is formed by R-L-C resonance, which is obviously related to R_E, L_E, and C_E. And the ω_0 denotes the angular oscillation frequency of the R-L-C circuit, and

$$\omega_0 = \sqrt{\frac{1}{L_E C_E} - \frac{1}{4}\gamma^2}, \tag{19}$$

where $\gamma = R_E/L_E$.

In the previous chapter, this paper also derived the expression for ω_0 through waveform simplification, which leads to the following equation:

$$\sqrt{\frac{1}{L_E C_E} - \frac{1}{4}\gamma^2} = \frac{\pi}{(1-D-D_Z)T - 2\Delta t}. \tag{20}$$

When the operating state is in the critical ZVS condition, R_E under this scenario is defined as R_{ZVS}, while C_E is defined as $C_{E,initial}$. The corresponding equation is expressed as:

$$\sqrt{\frac{1}{L_E C_{E,initial}} - \frac{R_{ZVS}^2}{4L_E^2}} = \frac{\pi}{(1-D)T - 2\Delta t}. \tag{21}$$

Therefore, once the rated load R is determined, R_{ZVS} can be calculated, and $C_{E,initial}$ can then be determined using formula (22).

$$C_{E,initial} = \frac{1}{\dfrac{\pi^2}{((1-D)T - 2\Delta t)^2} + \dfrac{R_{ZVS}^2}{4L_E^2}}. \tag{22}$$

To further clarify the design trade-offs, according to (15), the (22) can be expressed as:

$$C_{E,initial} = \frac{1}{\dfrac{4(U_{DS} - U_{DC})^2}{U_{DC}^2(DT - 2\Delta t)^2} + \dfrac{R_{ZVS}^2}{4L_E^2}}, \tag{23}$$

where the U_{DS} is the peak voltage on the MOSFET, and $U_{DS} = A + U_{DC}$.

As depicted in Fig. 13, increasing C_E decreases the ZVS margin D_Z until ZVS is no longer achieved, while decreasing C_E increases D_Z until it reaches the design value $D_{Z,ref}$. Therefore, the value of C_E can be determined through iterative simulations. According to the above analysis, the initial value for C_E can be determined by (22), significantly reducing the number of iterations required in simulations.

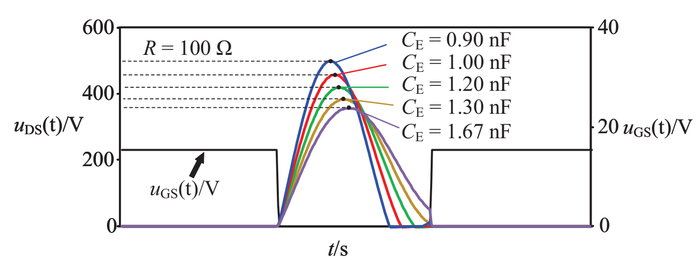

Fig. 13. The ZVS condition versus the value of C_E and equivalent load.

TABLE II
PARAMETERS OF PROPOSED CIRCUIT

Symbol	Definition	Value
C_E	Transmitting-side compensation capacitor	0.85 nF
C_1	Transmitting-side blocking capacitor	900 nF
C_2	Receiving-side compensation capacitor	0.969 nF
$L_{\mathrm{P},1}$	The inductance of the transmitting coil	19.497 μH
$L_{\mathrm{P},2}$	The inductance of the transmitting coil	19.213 μH
L_S	The inductance of receiving coil	31.074 μH
M_1	Mutual inductance	6.613 μH
M_2	Mutual inductance	7.172 μH
f_s	Operating frequency	1 MHz
E	Calculated amplitude of fundamental harmonic	179.74 V
U_DC	Input DC voltage	100 V
U_OUT	Output DC voltage	100 V
D	Duty cycle	0.55
D_Z	ZVS margin	0.08

C. Analysis of the Circuit and Parameters Design

Based on the equivalent circuit shown in Fig. 9 and the modeling of the output voltage of the proposed Class-E inverter, the input current of the transmitting coils can be expressed as follows:

$$|\boldsymbol{I}_\mathrm{P}| = \frac{|\boldsymbol{U}_{\mathrm{P},1}|}{|j\omega_\mathrm{s}L_\mathrm{E} + R_\mathrm{E}|} \approx \frac{E}{\omega_\mathrm{s}L_\mathrm{E}}, \tag{24}$$

where $\boldsymbol{I}_P$ represents the fundamental component of the input current for the transmitting coils, and $\boldsymbol{U}_{\mathrm{P},1}$ is the fundamental component of $u_{\mathrm{P},1}(t)$. The input to the coils can be approximated as a constant current source. Generally, under low coupling conditions with the coupling coefficient $k \leq 0.3$, the approximation accuracy of (24) is higher.

To simplify the compensation network and minimize power loss, the proposed circuit employs only capacitor C_2 for compensation. To determine the appropriate value for C_2 and the relationship between the circuit's input and output, Thevenin's and Norton's equivalent circuits are depicted in Fig. 11. The compensation capacitor C_2 should be resonant with the equivalent inductor L_S, as indicated in (25).

$$j\omega_\mathrm{s}L_\mathrm{S} = \frac{1}{j\omega_\mathrm{s}C_2}. \tag{25}$$

As shown in Fig. 11, the AC output voltage $\boldsymbol{U}_\mathrm{o}$ is independent of the load. The relationship between the input and output AC voltages is given by (26).

$$\boldsymbol{U}_\mathrm{o} = \frac{M_\mathrm{E}\boldsymbol{U}_{\mathrm{P},1}}{L_\mathrm{E}}. \tag{26}$$

Clearly, the output voltage is independent of the load. Consequently, the DC output voltage can be expressed as follows:

$$U_\mathrm{OUT} = \frac{\pi|\boldsymbol{U}_\mathrm{o}|}{4} = \frac{\pi M_\mathrm{E} E}{4L_\mathrm{E}}. \tag{27}$$

As detailed in the parameter determination process in Fig. 14, all circuit parameters are listed in Table II.

In practice, due to the parameter errors and parasitic parameters of passive components, we define the load-independent output range of the proposed circuit as 100 Ω to 1000 Ω. Fig. 15 presents the transfer gain curves under different loads, where $G(f) = U_\mathrm{OUT}/E$. It is evident that all curves intersect at the same point at a frequency of 1 MHz, confirming the load-independent characteristic of the transfer gain (output voltage) within the load range of 100 ohms to 1000 Ω.

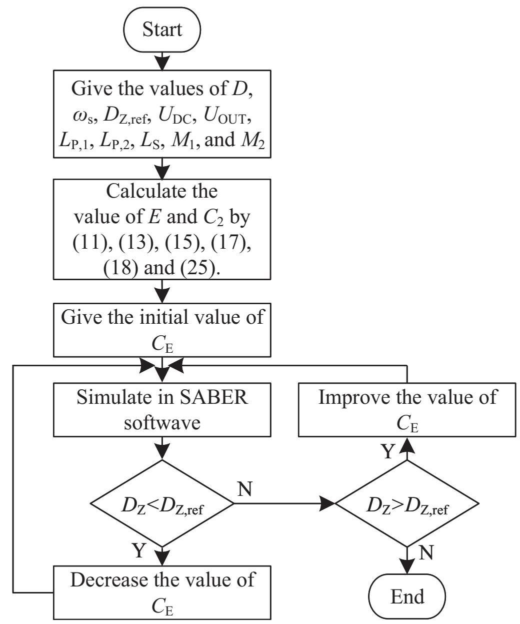

Fig. 14. The design process of the proposed circuit.

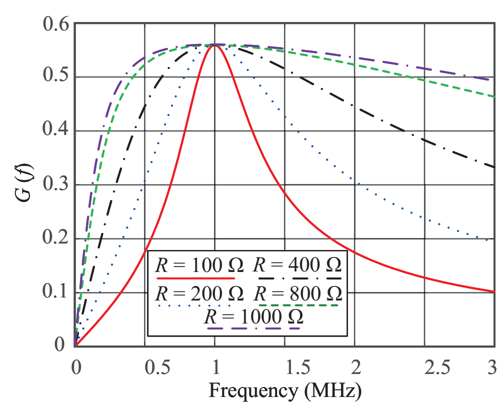

Fig. 15. The transfer gain of the proposed circuit.

In addition, the output performance under varying mutual inductance is provided in Fig. 16. Here, the total mutual inductance is expressed as $M = M_1 + M_2$, and all relevant parameters have undergone linearization processing.

Specifically, the mutual inductance under misalignment conditions is shown in Fig. 17. And the comparison between single-coil and dual-coil structures under misalignment conditions is presented in Fig. 18 and Fig. 19. In Fig. 18, the outer dimensions and transmission distance of the two coil schemes are kept consistent, and their receiving coils are identical. On this basis, the turn number of the single coil is adjusted to guarantee equal mutual inductance between the two structures under the aligned condition. In Fig. 19, M_T represents the mutual inductance of the single-coil structure, while $M = M_1 + M_2$ is defined as the total mutual inductance

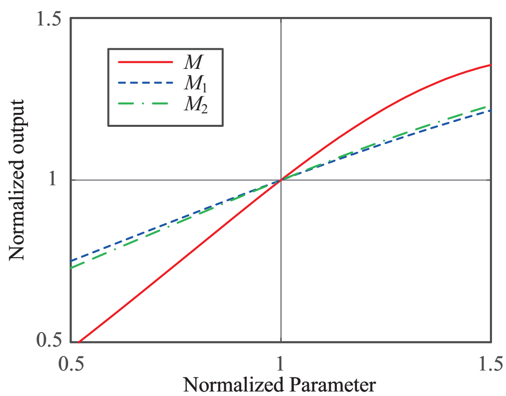

Fig. 16. Output versus mutual inductance.

of the dual-coil structure. Owing to the mutual inductance characteristics illustrated in Fig. 17, the equivalent mutual inductance of the dual-coil structure declines more slowly with misalignment as shown in Fig. 19.

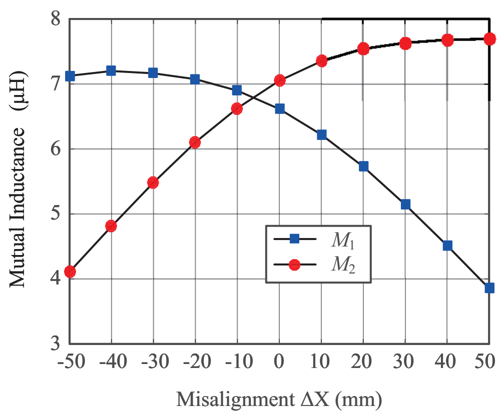

Fig. 17. Mutual inductance versus misalignment.

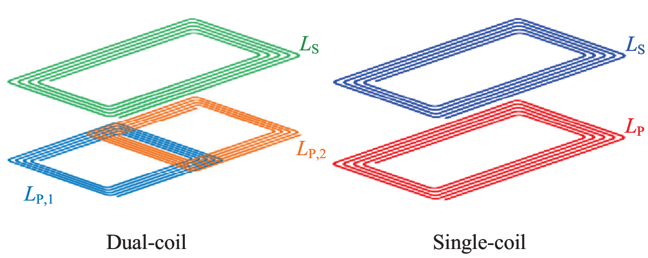

Fig. 18. Comparison of coil structures.

IV. Experimental Validation

To validate the analysis, a 100 W Class-E IPT prototype has been constructed, as illustrated in Fig. 20. This prototype includes a DC input, a transmitting circuit, a loosely coupled transformer, a receiving circuit, an oscilloscope, and an electronic load, labeled as components 1 through 6. As depicted in Fig. 20, the transmitting BP pad features two identical square coils, each with a side length of 165 mm.

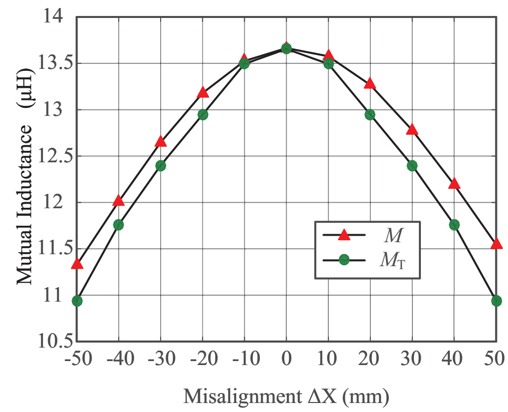

Fig. 19. Comparison of mutual inductance variation.

These coils overlap, with an overall length of 267 mm. The receiving coil is rectangular, measuring 267 mm in length and 165 mm in width. The coils form a loosely coupled transformer with a 45 mm gap between them. All coils are wound with Litz wire, 3 mm in diameter. The MOSFET used is a CGE1M120080, and the receiving-side rectifier circuit comprises four MBR20200 diodes. The electronic load is used to simulate the equivalent load.

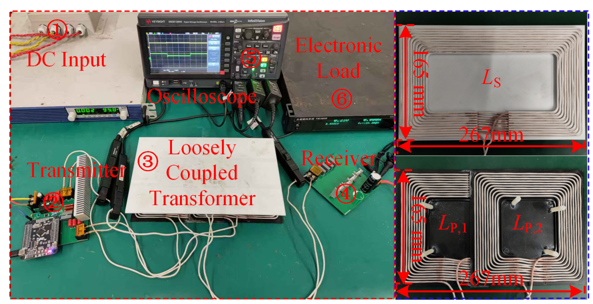

Fig. 20. Photograph of the proposed circuit.

Figs. 21(a) and (b) illustrate the soft-switching waveforms for equivalent loads of 100 Ω and 200 Ω, respectively. At an operating frequency of 1MHz and a 55% duty cycle, the measured amplitudes of $U_{\mathrm{DS}}(t)$ are 429 V for the 100 Ω load and 450 V for the 200 Ω load. The ZVS margin remains nearly constant despite variations in the load.

The currents through the BPQ-type coils are depicted in Fig. 22, demonstrating that the experimental waveform aligns with the theoretical waveform shown in Fig. 4. For a 100 Ω load, the experimental waveforms indicate AC root mean square (RMS) currents of 1.011 A in $L_{\mathrm{P},1}$ and 1.040 A in $L_{\mathrm{P},2}$. When the load is 200 Ω, the corresponding values are 1.041 A and 1.063 A, respectively. It proves that the transmitting coils are driven by a nearly CC power supply.

Fig. 23 displays the DC output U_{OUT} and I_{OUT} waveforms of the proposed circuit for varying equivalent loads. As the load R increases from 100 Ω to 200 Ω, the output voltage shifts from 100.70 V to 104.43 V, while the output current decreases from 1.007 A to 0.522 A. These results indicate that the output voltage remains nearly constant while the output current is halved. Additionally, Fig. 24 illustrates the output

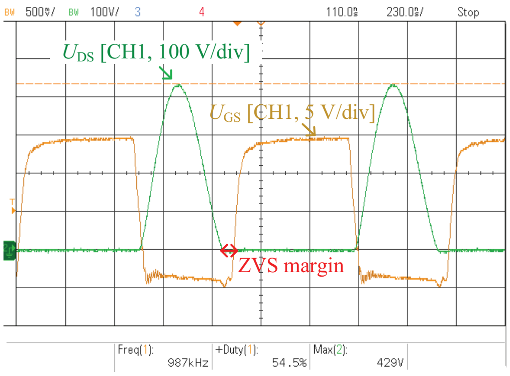

(a) $R = 100\ \Omega$

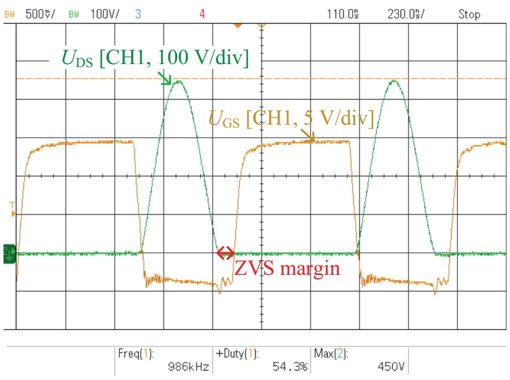

(b) $R = 200\ \Omega$

Fig. 21. Waveforms of ZVS.

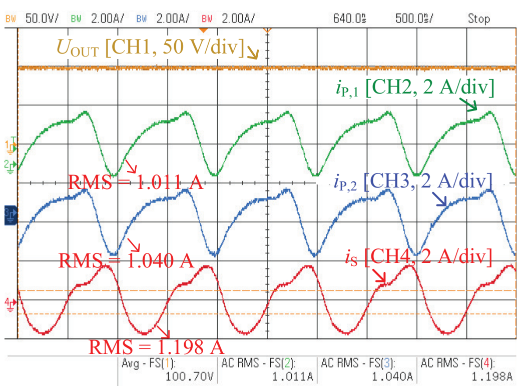

(a) $R = 100\ \Omega$

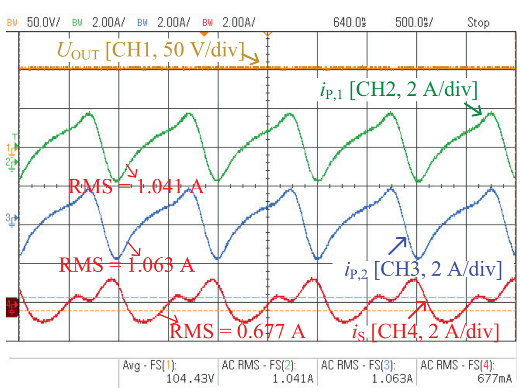

(b) $R = 200\ \Omega$

Fig. 22. Waveforms of the current in the coils.

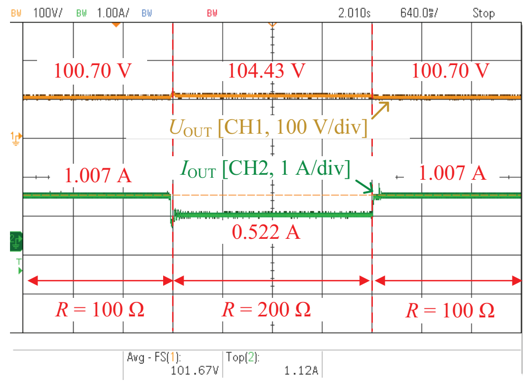

Fig. 23. Output waveforms when the load R changes.

voltage as the load gradually changes from 10% load (1000 Ω) to 100% load (100 Ω). This proves that the output voltage exhibits a certain load-independent characteristic.

Fig. 25 shows the efficiency performance of the proposed circuit from DC input to DC output. The results highlight the circuit's superior efficiency, with a maximum efficiency of approximately 93.2%.

Fig. 26 illustrates the loss distribution when the transfer power is 100 W. In the calculation process, the RMS values of currents were measured by current probes, the equivalent series resistance (ESR) values of coils and capacitors were tested by an LCR meter, and other data were obtained from relevant datasheets. Under the operating conditions shown in Fig. 26, it can be seen from the experimental results in Fig. 22 that the RMS current values flowing through Coils $L_{P,1}$, $L_{P,2}$ and L_S are 1.011 A, 1.040 A and 1.198 A, respectively, and the corresponding ESR values of these coils measured by the LCR meter are 0.440 Ω, 0.441 Ω and 0.676 Ω, respectively. Thus, the corresponding losses can be calculated as 0.45 W, 0.478 W, and 0.97 W. Similarly, the total loss of the capacitors can be calculated as 0.683 W. Since the MOSFET achieves ZVS, only the conduction loss and turn-off loss need to be counted for its loss calculation. In combination with the MOSFET datasheet and the measured values of the relevant currents, its conduction loss and turn-off loss are calculated as 0.2632 W and 2.2368 W, respectively. In addition, the forward voltage drop of the diodes in the rectifier bridge is 0.7 V, and the loss of the rectifier bridge is calculated to be approximately 1.44 W. The remaining losses are obtained by subtracting the above-mentioned losses from the total loss.

According to Fig. 26, the losses of the inverter account for approximately 44% of the total losses, thus yielding an inverter loss of about 3.21 W. Furthermore, the proposed inverter achieves an efficiency of roughly 97%.

V. Conclusion

This paper proposes a novel inductor-less Class-E inverter specifically designed for Inductive Power Transfer (IPT) systems with dual transmitting coils. The proposed method multiplexes the dual transmitting coils as inductors, completing the charging and discharging of the passive components while achieving quasi-constant current source excitation for the

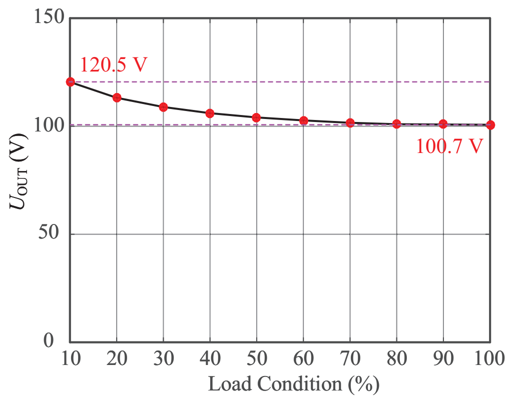

Fig. 24. The output voltage versus the load.

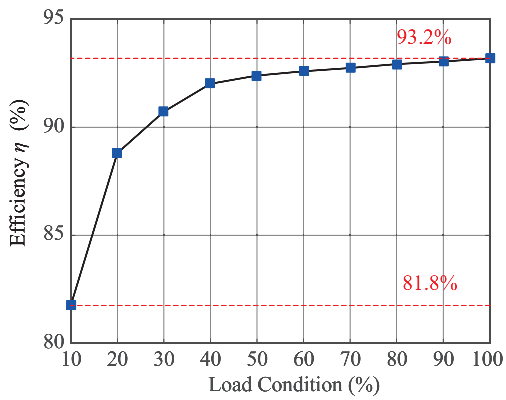

Fig. 25. Efficiency versus the load.

dual transmitting coils. Compared with the traditional Class-E inverter, the proposed method eliminates the inductors in the inverter and introduces the inherent advantages of the dual transmitting coil configuration. A prototype with a 100 V load-independent output voltage and 100 W output power has been developed. Experimental results demonstrate that the circuit achieves zero-voltage switching (ZVS) and maintains a load-independent output. The maximum efficiency observed is 93.2%. Compared with the full-bridge IPT circuit, although the proposed Class-E IPT circuit suffers from inflexible control schemes and relatively high switching stress, the proposed circuit features lower construction costs for the main circuit and driving control circuit, and its bridgeless configuration eliminates the risk of bridge arm shoot-through, thus exhibiting higher reliability.

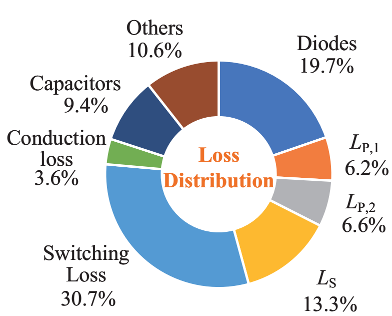

Fig. 26. Power loss distribution.

References

[1] C. Liu, X. Gao, and S. Cui, “A dual-layer receiver with low interlayer voltage stress and high power density for EVs wireless charging system,” *IEEE Trans. Ind. Electron.,* vol. 72, no. 4, pp. 3551–3561, Apr. 2025.

[2] Y. Gong, Z. Zhang, and S. Chang, “Single-transmitter-controlled multiple-channel constant current outputs for in-flight wireless charging of drones,” *IEEE Trans. Ind. Electron.,* vol. 71, no. 4, pp. 3606–3616, Apr. 2024.

[3] T. Feng, K. Shi, J. Jiang, and P. Wang, ”A solenoid magnetic coupler and its control method for omnidirectional wireless charging of UAVs,” *IEEE Trans. Ind. Electron.,* vol. 72, no. 3, pp. 2540–2550, Mar. 2025.

[4] J. Lee, B. Bae, B. Kim, J. Lim, and B. Lee, “A load-independent battery charging system for multiple wearable devices using conductive textile,” *IEEE Trans. Ind. Electron.,* vol. 71, no. 11, pp. 15211–15215, Nov. 2024.

[5] H. Zhang, C. K. Lee, and Z. Li, “Six degrees of freedom tracking and wireless charging for capsule endoscopy,” *IEEE Trans. Ind. Electron.,* vol. 72, no. 4, pp. 3643–3652, Apr. 2025.

[6] H. Zhang, W. Liu, Z. Li, and C. K. Lee, “Pulse frequency modulation of 3D wireless power transfer for capsule endoscopy,” *IEEE Trans. Ind. Electron.,* vol. 72, no. 1, pp. 308–317, Jan. 2025.

[7] H. Zhou, Z. Shen, Y. Wu, X. Chen, and Y. Zhang, “A stable dynamic electric vehicle wireless charging system based on triple decoupling receiving coils and a novel triple-diode rectifier,” *IEEE Trans. Ind. Electron.,* vol. 71, no. 10, pp. 12011–12018, Oct. 2024.

[8] Y. Zhang, C. Liu, M. Zhou, and X. Mao, “A novel asymmetrical quadrupolar coil for interoperability of unipolar, bipolar, and quadrupolar coils in electric vehicle wireless charging systems,” *IEEE Trans. Ind. Electron.,* vol. 71, no. 4, pp. 4300–4303, Apr. 2024.

[9] H. S. E. Mansour, M. Samir, B. Elhady, and S. Abdelmaksoud, “Wireless charging systems for electric vehicles: Review,” *Green Energy Intell. Transp.,* vol. 5, no. 5, Art. no. 100371, 2026.

[10] Y. Wu, U. K. Madawala, L. Zhao, and X. Dai, “Research status of bidirectional wireless power transfer technology,” *Green Energy Intell. Transp.,* vol. 5, no. 2, Art. no. 100266, 2026.

[11] B. Zhang *et al.*, “Design and implementation of interoperable high-efficiency bidirectional wireless power transfer systems for multiple vehicles,” *Green Energy Intell. Transp.,* vol. 5, no. 2, Art. no. 100307, 2026.

[12] W. V. Wang, D. J. Thrimawithana, and M. Neuburger, “An Si MOSFET-based high-power wireless EV charger with a wide ZVS operating range,” *IEEE Trans. Power Electron.,* vol. 36, no. 10, pp. 11163–11173, Oct. 2021.

[13] X. Zhu, Xing Zhao, and Yong Li, “High-efficiency WPT system for CC/CV charging based on double-half-bridge inverter topology with variable inductors,” *IEEE Trans. Power Electron.,* vol. 37, no. 2, pp. 2437–2448, Feb. 2022.

[14] Z. Sun, Y. Chi, Y. Wang, Y. Guan, and D. Xu, “Analysis and design of a high-frequency wireless battery charging system with smooth mode transition characteristics,” *IEEE Trans. Power Electron.,* vol. 38, no. 11, pp. 13273–13285, Nov. 2023.

[15] E. Chung and J. I. Ha, “Impedance matching network design for 6.78-MHz wireless power transfer system with constant power characteristics against misalignment,” *IEEE Trans. Power Electron.,* vol. 39, no. 1, pp. 1788–1801, Jan. 2024.

[16] S. Chen, Y. Chen, B. Zhang, and D. Qiu, ”Very-high-frequency resonant boost converter with wide output power range and synchronous drive,” *IEEE Trans. on Ind. Electron.,* vol. 70, no. 9, pp. 8928–8938, Sep. 2023.

[17] W. Qin, X. Wu, and J. Zhang, “Current-feed single-switch forward resonant DC transformer (DCX) with secondary diode-clamping,” *IEEE Trans. Ind. Electron.,* vol. 64, no. 10, pp. 7790–7799, Oct. 2017.

[18] H. P. Park and J. H. Jung, “Design methodology of quasi-resonant flyback converter with a divided resonant capacitor,” *IEEE Trans. Ind. Electron.,* vol. 68, no. 11, pp. 10796–10805, Nov. 2021.

[19] L. Zhang and K. Ngo, “A constant-current ZVS Class-E inverter with finite input inductance,” *IEEE Trans. Ind. Electron.,* vol. 68, no. 8, pp. 7693–7696, Aug. 2021.

[20] Z. Li, Q. Chen, S. Zhang, X. Ren, and Z. Zhang, “A novel domestic SEIH with high induction efficiency and compatibility of nonferromagnetic vessels,” *IEEE Trans. Ind. Electron.,* vol. 68, no. 9, pp. 8006–8016, Sep. 2021.

[21] R. E. Zulinski and K. J. Grady, "Load-independent class E power inverters: part I-Theoretical development," *Proc. IEEE Trans Circuits Syst.,* vol. 37, no. 8, pp. 1010–1018, Aug. 1990.
[22] A. Komanaka, W. Zhu, X. Wei, K. Nguyen, and H. Sekiya, "Generalized analysis of load-independent ZCS parallel-resonant inverter," *IEEE Trans. Ind. Electron.,* vol. 69, no. 1, pp. 347–356, Jan. 2022
[23] L. Roslaniec, A. S. Jurkov, A. A. Bastami, and D. J. Perreault, "Design of single-switch inverters for variable resistance/load modulation operation," *IEEE Trans. Power Electron.,* vol. 30, no. 6, pp. 3200–3214, Jun. 2015.
[24] S. Aldhaher, D. C. Yates, and P. D. Mitcheson, "Load-independent Class-E/EF inverters and rectifiers for MHz-switching applications," *IEEE Trans. Power Electron.,* vol. 33, no. 10, pp. 8270–8287, Oct. 2018.
[25] J. M. Arteaga, S. Aldhaher, G. Kkelis, D. C. Yates, and P. D. Mitcheson, "Multi-MHz IPT systems for variable coupling," *IEEE Trans. Power Electron.,* vol. 33, no. 9, pp. 7744–7758, Sep. 2018.
[26] Y. Komiyama, A. Komanaka, W. Zhu, A. Konishi, K. Nguyen, and H. Sekiya, "Analysis and design of load-independent series resonant power amplifier with constant current output and its application for WPT system," *IEEE Trans. Power Electron.,* vol. 39, no. 5, pp. 6515–6525, May 2024.
[27] Y. Cheng, Y. Guan, T. Yao, Y. Wang, W. Wang, and D. Xu, "Topology construction strategy of load-independent single-switch resonant inverter," *IEEE Trans. Ind. Electron.,* vol. 71, no. 9, pp. 10580–10590, Sep. 2024.
[28] Y. Huang, A. T. L. Lee, S. C. Tan, and S. Y. Hui, "Highly efficient wireless power transfer system with single-switch step-up resonant inverter," *IEEE J. Emerg. Sel. Topics Power Electron.,* vol. 9, no. 1, pp. 1157–1168, Feb. 2021.
[29] X. Huang, Z. Yu, Y. Dou, S. Lin, Z. Ouyang, and M. A. E. Andersen, "Load-Independent push-pull Class-E2 topology with coupled inductors for MHz-WPT applications," *IEEE Trans. Power Electron.,* vol. 37, no. 7, pp. 8726–8737, Jul. 2022.
[30] X. Huang, Y. Lin, Y. Dou, S. Lin, and J. Huang, "Load-independent push-pull Class-Φ2 inverter with single compact three-winding inductor," *IEEE Trans. Power Electron.,* vol. 38, no. 10, pp. 11916–11927, Oct. 2023.
[31] A. Zaheer, H. Hao, G. A. Covic, and D. Kacprzak, "Investigation of multiple decoupled coil primary pad topologies in lumped IPT systems for interoperable electric vehicle charging," *IEEE Trans. Power Electron.,* vol. 30, no. 4, pp. 1937–1955, Apr. 2015.
[32] Y. Li, T. Lin, R. Mai, L. Huang, and Z. He, "Compact double-sided decoupled coils-based WPT systems for high-power applications: analysis, design, and experimental verification," *IEEE Trans. Transp. Electrif.,* vol. 4, no. 1, pp. 64–75, Mar. 2018.
[33] H. Li, M. Liu, L. Kong, and Y. Wang, "An independent dual-coil driving topology for wireless power transfer," *IEEE Trans. Power Electron.,* vol. 38, no. 2, pp. 1378–1383, Feb. 2023.
[34] Y. Zhang, C. Liu, M. Zhou, and X. Mao, "A novel asymmetrical quadrupolar coil for interoperability of unipolar, bipolar, and quadrupolar coils in electric vehicle wireless charging systems," *IEEE Trans. Ind. Electron.,* vol. 71, no. 4, pp. 4300–4303, Apr. 2024.

Jingyu Wang received the B.Eng degree in electrical engineering and automation from Hefei University of Technology, Hefei, China, in 2019, the M.Eng. degree in electrical engineering from Qingdao University, Qingdao, China, in 2022, and the Ph.D. degree in control science and engineering from South China University of Technology, Guangzhou, China, in 2026.

He is currently an associate researcher with the School of Electrical Engineering, Qingdao University, Qingdao, China. His research interests include wireless power transfer, power electronics, and electric vehicles.

Hai Xu received the M.S. degree in agricultural engineering from South China Agricultural University, Guangzhou, China, in 2019, and the Ph.D. degree in power electronics from the South China University of Technology, Guangzhou, in 2024.

He is currently a Postdoctoral Fellow with the Department of Electrical and Electronic Engineering, The Hong Kong Polytechnic University, Hong Kong, China. His research interests include wireless power transfer, resonant power conversion, and magnetic coupler design.

Zhicong Huang (Senior Member, IEEE) received the B.Eng. degree in electrical engineering and automation and the M.Eng. degree in mechanical and electronic engineering from Huazhong University of Science and Technology, Wuhan, China, in 2010 and 2013, respectively, and the Ph.D. degree in power electronics from The Hong Kong Polytechnic University, Hong Kong, China, in 2018.

Since 2020, he has been an Associate Professor with Shien-Ming Wu School of Intelligent Engineering, South China University of Technology, Guangzhou, China. He was a Postdoctoral Fellow under the UM Macao Talent Program with the State Key Laboratory of Analog and Mixed-Signal VLSI, Macau, China, in 2019. His research interests include wireless power transfer, resonant power conversion, large-scale renewable power generation, artificial intelligence for power electronics, and wave energy converters.

Dr. Huang serves as an Associate Editor for IEEE Transactions on Consumer Electronics, IEEE Journal of Emerging and Selected Topics in Industrial Electronics and IEEE Open Journal of Power Electronics.

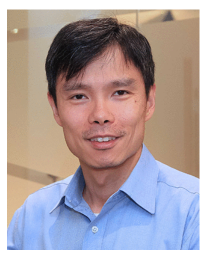

Chi-Kwan Lee (Senior Member, IEEE) graduated from the City University of Hong Kong, with B.Eng. and Ph.D. degrees in electronic engineering. He has held a Professorship since 2024, and is currently a Professor at the University of Technology Sydney, Australia, and Honorary Professor at the University of Hong Kong.

From 2008 - 2011, he was a lecturer in electrical engineering at the Hong Kong Polytechnic University. In 2012, he joined the University of Hong Kong, where he became an Associate Professor in 2018. He was a Visiting Researcher with Imperial College London, U.K. from 2010 - 2020. His research focuses include power converter design, electromagnetic device and wireless power transfer. Prof. Lee is a Senior Member of IEEE. He was a recipient of the 2015 IEEE Power Electronics Society Transactions First Prize Paper Award for his publications on Wireless Power Transfer. He serves on the steering committee and was the General Chair of 2018 IEEE PELS Workshop on Emerging Technologies: Wireless Power (WoW). He is an Associate Editor for the IEEE Transactions on Power Electronics and IEEE Journal of Emerging and Selected Topics in Power Electronics.

Io-Wa Iam (Member, IEEE) received the B.Sc. degree and Ph.D. degree in electrical and computer engineering from the University of Macau (UM), Macau, China, in 2020 and 2023, respectively. He is currently a Research Assistant Professor with the State Key Laboratory of Analog and Mixed-Signal VLSI and the Institute of Microelectronics, UM. Dr. Iam received the Macao Science and Technology R&D Award for Postgraduates (Ph.D. Level) in 2024. In 2019, he was awarded the "Best Track Paper Award" in APPEEC 2019. His current research interests include power electronics and wireless power transfer.

Chi-Seng Lam (Senior Member, IEEE) received the Ph.D. degree in electrical and electronics engineering from the University of Macau (UM), Macau, China, in 2012. He completed the Clare Hall Study Programme at the University of Cambridge, Cambridge, U.K., in 2019. In 2013, he was a Postdoctoral Fellow with The Hong Kong Polytechnic University, Hong Kong, China. He is currently a Full Professor with the State Key Laboratory of Analog and Mixed-Signal VLSI and the Institute of Microelectronics, UM, and also with the Department of Microelectronics, Faculty of Information Science and Computing, UM. He has coauthored or co-edited five books and more than 230 technical journals and conference papers. He holds six U.S. and ten Chinese patents. His research interests include power quality compensators, power management integrated circuits, wireless power transfer, and solar energy systems. Prof. Lam is currently the Founding Chair of the IEEE Macau IES Chapter, Founding Chair of the IEEE TEC Macau Chapter, and the Vice-Chair of the IEEE IES Technical Committee on Power Electronics. He currently serves as an Associate Editor for the IEEE Transactions on Power Electronics (TPEL), the IEEE Transactions on Industrial Electronics (TIE), the IEEE Transactions on Circuits and Systems – I: Regular Papers (TCAS-I), the IEEE Journal of Emerging and Selected Topics in Power Electronics (JESTPE), and the IEEE Open Journal of the Industrial Electronics Society (OJES). He was awarded the 2025 IEEE TPEL Associate Editor Excellence, 2025 IEEE JESTPE Star Associate Editor, 2024 IEEE TIE Outstanding Associate Editor, the 2024 IEEE TPEL Outstanding Reviewer, the 2024 and 2022 IEEE TIE Distinguished Reviewer, and the 2024 Outstanding Reviewer by the IEEE Solid State Circuits Society. Prof. Lam is a Fellow of The Institution of Engineering and Technology (IET).